Molecular Oxygen Abundance in Galactic Massive Star Formation Regions Based on SWAS Observations

Bing-Ru Wang[1,3] , Di Li[2,1,4,12] , Paul F. Goldsmith[5] , Jingwen Wu[3,1,12] , Chao-Wei Tsai[1,6] , Donghui Quan[4] , Xia Zhang[7] , Junzhi Wang[8] , Gary J. Melnick[9] , Jin-Zeng Li[1] , Gary A. Fuller[10,11] , and Jinjin Xie[1]

[1] National Astronomical Observatories, Chinese Academy of Sciences, Beijing 100101, China; dili@nao.cas.cn, jingwen@nao.cas.cn
[2] Tsinghua University, Beijing 100084, China
[3] University of Chinese Academy of Sciences, Beijing 100049, China
[4] Research Center for Astronomical Computing, Zhejiang Laboratory, Hangzhou 311100, China
[5] Jet Propulsion Laboratory, California Institute of Technology, Pasadena, CA 91109, USA
[6] Institute for Frontiers in Astronomy and Astrophysics, Beijing Normal University, Beijing 102206, China
[7] Xinjiang Astronomical Observatory, Chinese Academy of Sciences, Urumqi 830011, China
[8] Guangxi Key Laboratory for Relativistic Astrophysics, School of Physical Science and Technology, Guangxi University, Nanning 530004, China
[9] Center for Astrophysics, Harvard & Smithsonian, 60 Garden Street, MS 66, Cambridge, MA 02138, USA
[10] Jodrell Bank Center for Astrophysics, Department of Physics & Astronomy, University of Manchester, Oxford Road, Manchester, M13 9PL, UK
[11] I. Physikalisches Institut, University of Cologne, Zülpicher Str. 77, 50937 Köln, Germany

Abstract

Molecular oxygen abundance is a key parameter in understanding the chemical network of the interstellar medium. We estimate the molecular oxygen column density and abundance for a sample of Galactic massive star formation regions based on observations from the Submillimiter Wave Astronomy Satellite (SWAS) survey. We obtained an averaged O_2 spectrum based on this sample using the (SWAS) survey data (O_2, 487.249 GHz, $N = 3$–1, $J = 3$–2). No emission or absorption feature is seen around the supposed central velocity with a total integration time of $t_{\rm total} = 8.67 \times 10^3$ hr and an rms noise per channel of 1.45 mK. Assuming a kinetic temperature $T_{\rm kin} = 30$ K, we derive the 3σ upper limit of the O_2 column density to be 3.3×10^{15} cm^{-2}, close to the lowest values reported in Galactic massive star formation regions in previous studies. The corresponding O_2 abundance upper limit is 6.7×10^{-8}, lower than all previous results based on SWAS observations and is close to the lowest reported value in massive star formation regions. On a galactic scale, our statistical results confirm a generally low O_2 abundance for Galactic massive star formation regions. This abundance is also lower than results reported in extragalactic sources.

Key words: ISM: molecules – galaxies: abundances – ISM: lines and bands – Galaxy: abundances

1. Introduction

In the interstellar medium (ISM), the most abundant species, such as H, H_2, O, C^+, and N in diffuse clouds and H_2, CO, and N_2 in molecular clouds (Tielens 2013, with He not included), are composed of the most abundant elements and often play important roles in both the chemical and physical evolution of the ISM. In turn, the resulting chemical composition affects the energy transfer processes in the ISM. The formation and evolution of these species are highly dependent on the (kinetic) temperature, volume density and radiation field in the ISM. Star formation is an important process in the ISM evolution, with the feedback from the forming and formed stars often setting these parameters and, thus, influencing the most abundant molecular species in molecular clouds other than H_2/H and He. Oxygen is the third most abundant element in the universe (Heiles 1971; Dalgarno & McCray 1972). O-bearing species

are among the most abundant ones in both the diffuse clouds and the molecular clouds where the stars form. Thus, it is necessary to study the existing forms of oxygen in ISM and their abundance.

In diffuse gas subject to a strong interstellar far-ultraviolet (FUV) radiation field, oxygen and carbon atoms are predominantly ionized (Yamamoto 2017). With an ionization potential greater than that of hydrogen, in dense molecular gas where the FUV field is attenuated by dust absorption, elemental oxygen can exist within simple molecular species whose abundance and distribution are determined by gas-phase densities and temperatures, or by freezeout and surface chemistry on interstellar dust grains (Hollenbach et al. 2009; van Dishoeck et al. 2013; Wang et al. 2015; Zhang et al. 2020). Early theoretical calculations suggested that within well-shielded clouds, molecular oxygen (O_2), along with gas-phase H_2O, could be abundant reservoirs of elemental oxygen (Herbst & Klemperer 1973; Langer 1976) as well as major gas coolants

---

[12] Corresponding author.

(Goldsmith & Langer [1978]). Because transitions between low-lying O_2 energy levels can be easily excited collisionally by H_2 at typical dense molecular cloud temperatures, molecular oxygen was once predicted to be comparable to CO and H_2O as a dominate molecular cloud gas coolant (Goldsmith & Langer [1978]; Neufeld et al. [1995]). Though no longer thought to be a major gas coolant, the abundance of molecular oxygen remains a largely unanswered question, with relevance to our understanding of interstellar chemistry.

Attempts to observe Galactic sources of O_2 from the best mountaintop or airborne telescopes are prevented by the significant presence of O_2 in our own atmosphere. To avoid this obstacle, efforts have been made to observe highly redshifted O_2 from extragalactic sources (Goldsmith & Young [1989]; Combes et al. [1991], [1997]; Wang et al. [2020]) as well as the isotopologue $^{16}O^{18}O$ toward Galactic sources (Goldsmith et al. [1985]; Taquet et al. [2018]). However, the best prospects for detecting O_2 remain a space-based telescope, well above the blocking effects of Earth's atmosphere. Observations with the Submillimiter Wave Astronomy Satellite (SWAS, Melnick et al. [2000]), the Odin satellite (Frisk et al. [2003]; Nordh et al. [2003]), and the Herschel Space Observatory (Pilbratt et al. [2010]) have confirmed a much lower O_2 abundance (upper limit) in Galactic dense gas (generally from 5×10^{-8} to 10^{-6}), more than 2 orders of magnitudes below the earlier predictions of cold-cloud gas-phase chemical models (Goldsmith et al. [2000], [2011]; Pagani et al. [2003]; Bergin & Melnick [2005]; Larsson et al. [2007]; Sandqvist et al. [2008], [2015]; Liseau et al. [2012]; Yildiz et al. [2013]; Chen et al. [2014]; Wirström et al. [2016]). The only two Galactic O_2 detections in Orion (Goldsmith et al. [2011]; Chen et al. [2014]) and Rho Ophiuchi A (Rho Oph A, with a tentative detection included) (Goldsmith et al. [2002]; Larsson et al. [2007]; Liseau et al. [2012]) are both local warm spots which are likely heated by shocks, resulting in enhanced O_2 emission due to the release of O_2 from grain surfaces (Goldsmith et al. [2011]; Liseau et al. [2012]; Chen et al. [2014]) or, alternately, from gas-phase chemistry within the postshocked regions behind FUV-illuminated shocks (Melnick & Kaufman [2015]). Generally, the corresponding O_2 abundance values are less than 10^{-7} relative to H_2. The limited postshock distances over which the O_2 abundance is enhanced combined with geometric effects—i.e., the angle the shock presents to the observer—may be reasons confirmed O_2 detections are rare (Melnick & Kaufman [2015]). Similar shock enhancement mechanisms may also apply to extragalactic sources, such as the ultra-luminous infrared galaxy Mrk 231, which led to a detection with an inferred O_2 abundance greater than 1×10^{-4} (Wang et al. [2020]). Within the central region of MrK 231 and other observed extragalactic sources such as the Small Magellanic Cloud (SMC), NGC 6240 and B0218+357, the O_2 abundance remains very low, comparable to the Galactic sources (Wang et al. [2020]; Wilson et al. [2005]; Combes et al. [1991], [1997]).

The O_2 abundance is commonly very low in dense molecular gas and the significant surplus of oxygen in solar abundance (the interstellar "O crisis," Whittet [2010a]) remains. Obtaining improved constraints on the upper limit to the O_2 abundance from the non-detections toward Galactic massive star formation regions provides critical data for time-dependent gas-grain interstellar chemistry models (Zhang et al. [2020]) and can help us gain a better understanding of the oxygen life-cycle in the Galaxy (Vastel et al. [2002]; Whittet et al. [2010]; Whittet [2010b]).

In this paper, we estimate the average molecular oxygen upper limit based on a large sample of Galactic massive star formation regions using the SWAS survey data. The paper is organized as follows: in Section [2] we briefly describe the SWAS survey observations and data; in Section [3] we describe our data reduction steps; The results are presented in Section [4]. We compare our results with previous studies in Section [5]. Finally, in Section [6] we present our conclusions.

2. SWAS Observation

The SWAS mission lasted for 5.5 yr and the survey covers hundreds of Galactic molecular clouds (Bergin & Melnick [2005]). The sources are observed at single or multiple positions via intermittent sampling. For every observed position, four molecular lines were observed simultaneously by two double sideband receivers (DSBs), Receiver 1 (C I, $^3P_1-^3P_0$, 492.161 GHz; O_2, 3,3–1,2, 487.249 GHz) and Receiver 2 (H_2O, $1_{10} - 1_{01}$, 556.936 GHz; ^{13}CO ($J = 5$–4, 550.926 GHz[13])), respectively (Melnick et al. [2000]). The SWAS's beam size is $3.'5 \times 5.'0$ for Receiver 1 and $3.'3 \times 4.'5$ for Receiver 2 and the main beam efficiency is 0.90 (Melnick et al. [2000]). We obtained the data of all 386 sources from the SWAS spectrum service in NASA/IPAC infrared science archive.[14]

3. Data Reduction

We assumed that for every observed position in the SWAS survey, the C I line ($^3P_1-^3P_0$, 492.161 GHz) and O_2 line (3,3–1,2, 487.249 GHz) sampled simultaneously by Receiver 1 have the same central velocities. Previous Galactic O_2 detections are consistent with this assumption (see Appendix [A]). This assumption that C I and O_2 share the same central velocity is consistent with the C I and O_2 line observation results of the only two previous Galactic O_2 detection cases in the Rho Oph A (Larsson et al. [2007]; Liseau et al. [2012]) and Orion (Goldsmith et al. [2011]) molecular clouds (see Appendix [A] for more details).

We analyzed the C I and O_2 spectra of the observed massive star formation regions in the SWAS survey, but excluded the

---

[13] For a few sources, observations of $H_2^{18}O$ ($1_{10}-1_{01}$, 547.676 GHz) were also performed toward some positions instead.
[14] http://irsa.ipac.caltech.edu/applications/SWAS/SWAS/list.html

sources in the Orion molecular cloud[15] and near/toward the Galactic center.[16] We selected positions whose C I spectra have only one clear single emission peak to prepare our sample for statistical analysis. To lower the influence by the weighting differences among spectra due to different integration times, we only selected positions with long enough total integration time (not less than 10,000 s, on+off, see Appendix D) and used on the corresponding O_2 and C I spectra to compose the overall averaged O_2 and C I spectra. Subsequently, based on the overall averaged spectra, we estimate a statistical O_2 abundance upper limit.

For every observed position, all sampled C I and O_2 spectra were combined to generate the corresponding C I and O_2 average spectra, respectively. The C I average spectrum was fitted with a Gaussian and the centroid velocity was adopted as the central velocity of the corresponding O_2 average spectrum. This central velocity was aligned to $0 \, \mathrm{km \, s^{-1}}$ in our spectral plots. The antenna temperatures were then corrected for the SWAS's main beam efficiency of 0.90. Then a linear baseline was fitted based on spectra outside the -20 to $20 \, \mathrm{km \, s^{-1}}$ velocity interval, and was subtracted from the spectra. The average spectra of different positions were then combined to generate an overall O_2 average spectrum and corresponding C I average spectrum for the sample of massive star formation regions. The operations above were performed using the GILDAS CLASS software. Considering the varying integration times among different observed positions, the mode of "weighting by time"[17] was adopted.

4. Results and Analysis

4.1. Overall Averaged O_2 and C I Spectra

The observed positions in the massive star formation regions analyzed in this paper are listed in Table D1 in Appendix D. The overall total integration time (on+off) is $3.12 \times 10^7 \, \mathrm{s}$ ($8.67 \times 10^3 \, \mathrm{hr}$). The long-term integration ability of SWAS receivers has been investigated and confirmed in Wang et al. (2024) and a noise floor has not been reached even after such a long total integration time.

Figure 1 shows the O_2 and C I overall averaged spectra of these observed positions, with the assumed central velocities aligned to $0 \, \mathrm{km \, s^{-1}}$. In the averaged O_2 spectra, there is no obvious emission or absorption feature around the central velocity. The rms noise per channel is $1.33 \times 10^{-3} \, \mathrm{K}$, which is very close to the theoretical value $1.24 \times 10^{-3} \, \mathrm{K}$. The corresponding overall averaged C I has a clear single emission peak. The central velocity is $0.010 \pm 0.016 \, \mathrm{km \, s^{-1}}$ and the line width (full width at half maximum, FWHM) is $6.3 \pm 0.043 \, \mathrm{km \, s^{-1}}$ according to the Gaussian fitting results.

4.2. Molecular Oxygen Column Density and Abundance Upper Limit

4.2.1. O_2's Radiative Transitions, Collision Excitation and Thermalization

As a homonuclear molecule, O_2 has no permanent electric dipole moment and thus has no pure rotational transitions (Kaiser et al. 1999) (i.e., electric-dipole rotational transitions, Listz & Vanden Bout 1985). However, the coupling of the electron spin angular momentum of the unpaired electrons (designated as S, whose associated moment is a purely magnetic dipole moment, Gordy & Cook 1984) and the non-spin angular momentum (designated as N, see Gordy & Cook 1984) causes the splitting of N and thus generates the resultant total angular momentum J (exclusive nuclear spin, according to Gordy & Cook 1984). The transitions allowed between J and/or N levels are magnetic dipole transitions, with the selection rules being $\Delta N = 0, \pm 2$ and $\Delta J = 0, \pm 1$ (Maréchal et al. 1997; Brown & Carrington 2003).

The allowed radiative transitions between the lowest 48 energy levels all have small spontaneous emission coefficients (10^{-10}–$10^{-7} \, \mathrm{s^{-1}}$, Drouin et al. 2010). For lower O_2 energy levels, these slow rates make the radiative transitions between them have relatively low critical densities and thus easily thermalized. The low transition strength and low molecular oxygen abundance make the $487 \, \mathrm{GHz}$ O_2 (3,3–1,2) transition almost certainly optically thin.

SWAS generally observed the dense molecular cloud with molecular hydrogen volume density (number density) $n_{H_2} > 10^3 \, \mathrm{cm^{-3}}$ (Melnick 1995). When $n_{H_2} \geqslant 10^3 \, \mathrm{cm^{-3}}$ and the kinetic temperature $T_{\mathrm{kin}} \leqslant 30 \, \mathrm{K}$, O_2 (3,3) levels are essentially thermalized (Goldsmith et al. 2000). Further calculations suggested that $n_{H_2} > 10^3 \, \mathrm{cm^{-3}}$ is enough to keep the (3,3) energy level, with the upper energy level being close to local thermal equilibrium (LTE) at a temperature of $100 \, \mathrm{K}$ (Goldsmith et al. 2011).

For the massive star formation regions we analyzed in the SWAS survey, on average we can expect even higher H_2 volume density but not likely higher kinetic temperature. To estimate the average O_2 column density and abundance upper limits, we adopted the median values of H_2 volume density and T_{kin} of seven giant cloud cores from Table 1 in Goldsmith et al. (2002) as the assumed average values for the sample of massive star formation regions. The seven giant cloud cores are Mon R2, M17SW, W49, W51, S140, Cep A and NCG 7538, respectively.[18] All of them had been studied individually based on SWAS O_2 (3,3–1,2) and Five College Radio Astronomical Observatory (FCRAO) $C^{18}O$ $J = 1$–0 observations in Goldsmith et al. (2000) and were also in our sample in this paper. With the H_2 volume density and T_{kin}

---

[15] With O_2 detected in previous study (Goldsmith et al. 2011).

[16] It is hard to fix the C I central velocity at these positions.

[17] See www.iram.fr/IRAMFR/GILDAS/doc/pdf/class.pdf.

[18] For W33, DR 21 and DR 21(OH) which are massive star formation regions and were also observed in Goldsmith et al. (2000), since their SWAS C I spectra do not have a clear single peak, they were not included in our sample in this paper and their parameters were not adopted.
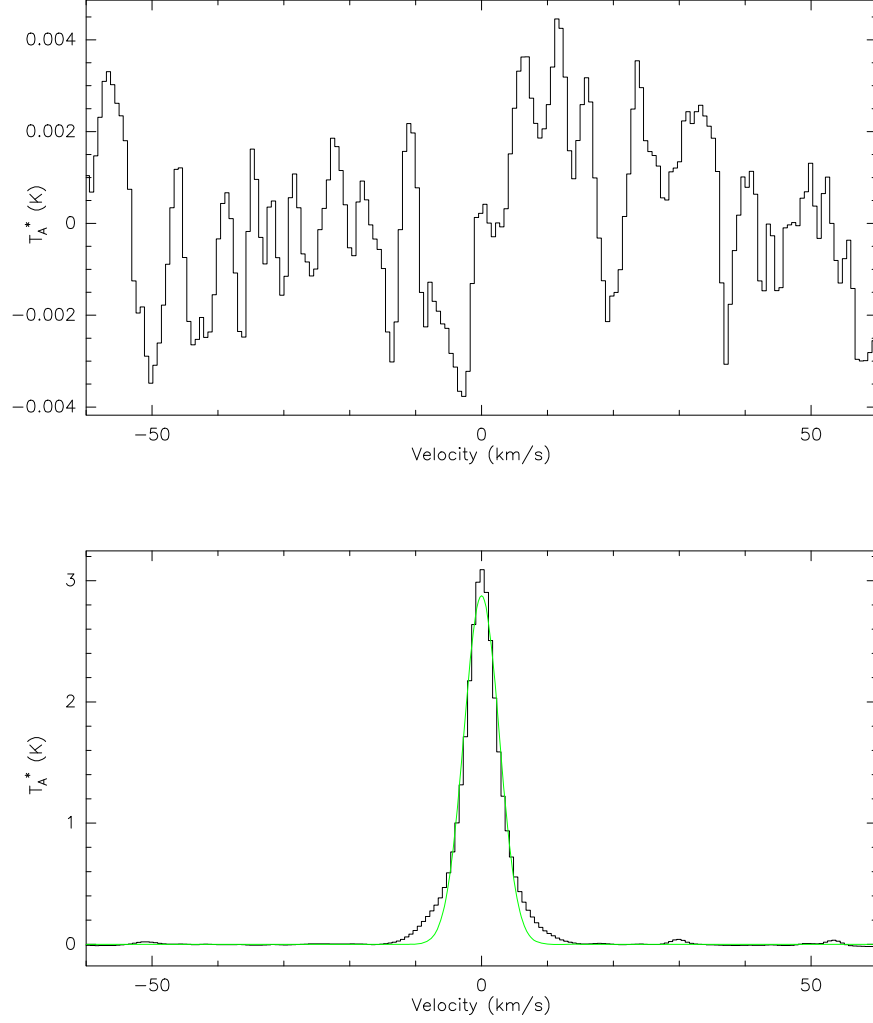
Figure 1. Overall averaged O_2 spectrum of observed positions in Table D1 in Appendix D (upper panel) and the corresponding overall averaged C I spectra (lower panel). The rms noise per channel of the O_2 spectrum (based on the channel values in the intervals $[-50, -20]$ and $[40, 60]$ km s^{-1}) is 1.33×10^{-3} K. The green solid line shows the Gaussian fitting result of the C I spectrum, with central velocity of 0.010 ± 0.016 km s^{-1} and line width of 6.3 ± 0.043 km s^{-1}.

values adopted as described above, we assumed an average n_{H_2} $= 10^{5.6}$ cm^{-3} and average $T_{kin} = 30$ K for the sample of massive star formation regions in our estimations in this paper. We adopted the line width (FWHM) of the corresponding overall averaged C I spectrum (see Figure 1) as the assumed line width of the overall averaged O_2 spectrum of this sample. With these assumed average n_{H_2}, T_{kin} and line width of the overall averaged O_2 spectrum, we performed Radex non-LTE analysis (Van der Tak et al. 2007) for O_2 total column densities of 10^{13}, 10^{14}–10^{18} cm^{-2}. The O_2 fractional populations of the (3,3) energy level are all 0.128, the same as in LTE while the (3,3–2,1) transition is always optically thin, as expected.

4.2.2. Average O_2 Column Density Upper Limit for Galactic Massive Star Formation Regions

When O_2 (3,3) energy is thermalized, for the O_2 (3,3–2,1) transition, its excitation temperature $T_{ex} \simeq T_{kin}$. Assuming the observed molecular clouds fill the SWAS beam, when the background continuum radiation at 2.73 K is ignored, O_2 column density at energy level (3,3), the upper level of the 487 GHz O_2 transition in the quasi-Planck case (see Appendix B), is

$$N_u^{\text{quasi-Planck}-\text{no}-\text{bg}} = \frac{8\pi k\nu^2}{hc^3 A_{ul}} \int T_{mb} dv. \tag{1}$$

The O_2 total column density is

$$N_{\text{tot}}^{\text{quasi-Planck}-\text{no}-\text{bg}} = \text{CF} \cdot \frac{8\pi k \nu^2}{hc^3 A_{\text{ul}}} \int T_{\text{mb}} dv. \qquad (2)$$

Here A_{ul} is the Einstein A coefficient, and CF is the correction factor, the inverse of the fractional population of a given level. For the thermalized O_2 (3,3) level in our calculation, CF = 1/ 0.128 = 7.81. (see Section 4.2.1).

The 3σ integrated line intensity upper limit for the overall averaged O_2 spectrum in Figure 1 is

$$\int T_{\text{mb}} dv = 3\sigma_{O_2} \sqrt{\delta v \Delta v}, \qquad (3)$$

according to Pagani et al. (2003). $\sigma_{O_2} = 1.33 \times 10^{-3}$ K is the rms noise per channel of the overall averaged O_2 spectrum, $\delta v = 0.64 \, \text{km s}^{-1}$ is the velocity resolution and Δv is the assumed line width, taken as $6.3 \, \text{km s}^{-1}$ (see more in Appendix C.2), which is the line width of the corresponding overall averaged C I spectrum. With A_{ul} of O_2 (3,3–1,2) as $8.66 \times 10^{-9} \, \text{s}^{-1}$ (Drouin et al. 2010), the 3σ average O_2 column density upper limit is $3.3 \times 10^{15} \, \text{cm}^{-2}$.

With corrections for the O_2 rms noise per channel and then for the assumed O_2 line width, this column density upper limit at 30 K is $3.3 \times 10^{15} \, \text{cm}^{-2}$ (see Appendices C.1 and C.2). For thermalized O_2 (3,3) level at $T_{\text{kin}} = 20\text{–}40$ K, O_2 column density upper limit is 1.0–1.05 times the abundance value at this assumed $T_{\text{kin}} = 30$ K (see Appendix C.3).

4.2.3. Averaged O_2 Column Abundance Upper Limit for Galactic Massive Star Formation Regions

We used the weighted (integrated intensity) ratio method in Goldsmith et al. (2000) to estimate a 3σ limit for the averaged O_2 abundance in Galactic massive star formation regions. In principle, it derives the fractional abundance of O_2 from the $C^{18}O$ fractional abundance value through the ratio of their column density $N(O_2)/N(C^{18}O)$

$$\frac{N(O_2)}{N(H_2)} = \frac{N(O_2)}{N(C^{18}O)} \cdot \frac{N(C^{18}O)}{N(H_2)}$$
$$= \frac{N(O_2)}{N(C^{18}O)} \cdot X_{C^{18}O}. \qquad (4)$$

The $C^{18}O$ total column density can be calculated from the corresponding $C^{18}O$ $J = 1\text{–}0$ (109.782 GHz) spectrum (Goldsmith et al. 2000), also using Equation (2)

$$\frac{N(O_2)}{N(C^{18}O)} = \left[\frac{\nu^2(O_2, 3_3 - 1_2)}{\nu^2(C^{18}O, 1-0)} \frac{A_{\text{ul}}(C^{18}O, J = 1)}{A_{\text{ul}}(O_2, 3_3 - 1_2)} \right]$$
$$\cdot \frac{\text{CF}(O_2, 3_3)}{\text{CF}(C^{18}O, J = 1)} \cdot R_T^W. \qquad (5)$$

R_T^W is the ratio of O_2 integrated line intensity and $C^{18}O$ integrated line intensity, weighted by the $C^{18}O$ main beam brightness temperature in each channel when both O_2 and $C^{18}O$

spectra share the same velocity resolution. $A_{\text{ul}}(C^{18}O, J = 1)$ and $A_{\text{ul}}(O_2, 3_3 - 1_2)$ are the Einstein A coefficients for the $C^{18}O$ $J = 1$ and O_2 (3,3–1,2) transitions, respectively.

$$R_T^W = \frac{\sum_i T_{\text{mb}}(O_2, 3, 3-1, 2)_i T_{\text{mb}}(C^{18}O, 1-0)_i}{\sum_i T_{\text{mb}}(C^{18}O, 1-0)_i T_{\text{mb}}(C^{18}O, 1-0)_i}, \qquad (6)$$

according to Goldsmith et al. (2000).

For the overall averaged O_2 spectra without any feature around the supposed central velocity, we derive a 3σ upper limit for the averaged O_2 abundance from the uncertainty of the weighted ratio.

The $C^{18}O$ abundance corresponds to the entire $C^{18}O$ $J = 1\text{–}0$ integrated intensity. It also corresponds to the weighted integrated line intensity of $C^{18}O$ $J = 1\text{–}0$ in Equation (6). The O_2 rms noise per channel is the rms uncertainty in one channel and the corresponding weighted rms uncertainty of O_2 line intensity in a single channel is

$$\sigma_{O_2} \sqrt{\frac{\sum_i T_{\text{mb}}^2(C^{18}O, 1-0)_i}{n}}. \qquad (7)$$

σ_{O_2} is the rms noise per channel of the overall averaged O_2 spectrum $(1.33 \times 10^{-3}$ K) at its velocity resolution $0.64 \, \text{km s}^{-1}$. n is the total number of the channels that were taken into account for the O_2 integrated line intensity. For random noise in independent O_2 channels, the weighted rms uncertainty of O_2 integrated line intensity is

$$\sigma_{O_2} \sqrt{\frac{\sum_i T_{\text{mb}}^2(C^{18}O, 1-0)_i}{n}} \cdot \sqrt{n}$$
$$= \sigma_{O_2} \sqrt{\sum_i T_{\text{mb}}^2(C^{18}O, 1-0)_i}. \qquad (8)$$

Then the weighted rms uncertainty of the ratio of O_2 and $C^{18}O$ integrated line intensity is

$$\sigma_{R_T^{\text{wg}}} = \frac{\sigma_{O_2} \sqrt{\sum_i T_{\text{mb}}^2(C^{18}O, 1-0)_i}}{\sum_i T_{\text{mb}}(C^{18}O, 1-0)_i T_{\text{mb}}(C^{18}O, 1-0)_i}$$
$$= \frac{\sigma_{O_2}}{\sqrt{\sum_i T_{\text{mb}}^2(C^{18}O, 1-0)_i}}. \qquad (9)$$

The overall averaged C I has a near-Gaussian profile. Assuming a Gaussian line profile for the supposed corresponding $J = 1\text{–}0$ $C^{18}O$ spectrum, we obtain

$$\sigma_{R_T^{\text{wg}}} = \frac{\sigma_{O_2}}{\sqrt[4]{\frac{\pi}{8 ln2}} T_{0, C^{18}O, 1-0} \sqrt{\frac{\Delta v_{\text{FWHM}, C^{18}O, 1-0}}{\delta v_{O_2}}}}, \qquad (10)$$

with $T_{0, C^{18}O, 1-0}$ and $\Delta v_{\text{FWHM}, C^{18}O, 1-0}$ as the peak temperature and the line width (FWHM) of the overall averaged $C^{18}O$ (1–0) spectrum, respectively. δv_{O_2} is the channel width of the overall averaged O_2 spectrum, the same as the velocity resolution in Equation (3). Equation (10) is the analytical expression of Equation(4) in Goldsmith et al. (2000).
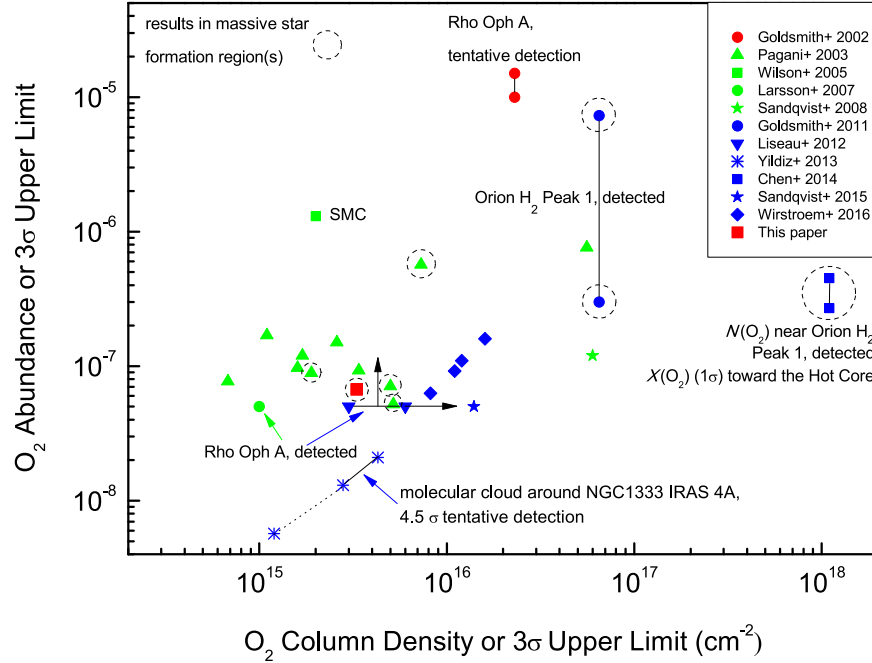
Figure 2. O_2 column density and abundance upper limits (3σ) in Galactic and SMC (Wilson et al. 2005). The observed targets circled in black dashed lines are in massive star formation regions. Symbols in red, green, and blue represent results based on observations via SWAS, and the Odin and Herschel telescopes, respectively. The symbols linked with solid black lines are O_2 detected cases or tentative detections, showing the ranges. Symbols linked by a dotted black line represent results of different positions for the same object in the same study. The black arrows suggest the possible lower limit.

We adopted the median of $T_{0,\text{C}^{18}\text{O},1-0}$ values (1.1 K in 0.8–1.3 K) for the seven Galactic giant molecule cloud cores[19] described in Section 4.2.1 as the assumed $T_{0,\text{C}^{18}\text{O},1-0}$ of the corresponding overall averaged C^{18}O (1–0) spectrum under the same spatial resolution as SWAS. The $\Delta v_{\text{FWHM},\text{C}^{18}\text{O}}$ values of the giant molecular cloud cores were not listed in Goldsmith et al. (2000). We adopted the line width of the overall averaged C I spectra, 6.3 km s^{-1}, as the assumed corresponding C^{18}O $J=1-0$ line width.

We performed Radex non-LTE analysis (Van der Tak et al. 2007) for C^{18}O total column densities of 10^{14}, 10^{15}–10^{18} cm^{-2} at $T_{\text{kin}}=30$ K, $n_{\text{H}_2}=10^{5.6}$ cm^{-3} as assumed in Section 4.2.1. The C^{18}O population of the $J=1$ energy level is from 0.221 to 0.216, all being very close to the value 0.215 when it is in LTE. We adopted $\text{CF}(\text{C}^{18}\text{O}, J=1)=4.54$ (from the results for $N(\text{C}^{18}\text{O})=10^{16}$ cm^{-2} in Radex non-LTE analysis) in our calculation.

Instituting three times Equation (10) into Equation (5) together with $A_{\text{ul}}=6.266\times10^{-8}$ s^{-1} for C^{18}O (1–0) (from the Leiden Atomic and Molecular Database[20]) and $X_{\text{C}^{18}\text{O}}=1.7\times10^{-7}$ (Frerking et al. 1982), we derived a 3σ average

O_2 abundance upper limit as 5.6×10^{-8} for Galactic massive star formation region.

With corrections for the O_2 rms noise per channel and then for the assumed C^{18}O $J=1-0$ line width, this abundance upper limit at 30 K is corrected to 6.7×10^{-8} (see Appendices C.1 and C.2). When the C^{18}O ($J=1$) and O_2 (3,3) levels are both thermalized, at $T_{\text{kin}}=20$–40 K, the O_2 abundance upper limit is 0.8–2.1 times this value at the assumed $T_{\text{kin}}=30$ K (see Appendix C.3).

5. Discussion

With total integration time (on+off) of 3.12×10^7 s and rms noise per channel as 1.45×10^{-3} K, we derived the 3σ average O_2 column density upper limit as 3.3×10^{15} cm^{-2} and O_2 abundance upper limit as 6.7×10^{-8} for Galactic massive star formation regions based on SWAS survey data. The values are lower than the previous values based on SWAS observations toward individual sources or regions in Goldsmith et al. (2000)[21] and Goldsmith et al. (2002).

Figure 2 shows O_2 column density and abundance or their 3σ upper limits in previous studies, together with the values derived in this paper. The results are for Galactic sources and SMC (Wilson et al. 2005). The observed targets circled in

---

[19] See Table 1 in Goldsmith et al. (2000), based on FCRAO C^{18}O (1–0) data convolved to 4′.4 SWAS FWHM beam.
[20] https://home.strw.leidenuniv.nl/moldata/datafiles/c18o.dat

---

[21] No column density values were presented in Goldsmith et al. (2000), see Table E1 in Appendix E.

black dashed lines are in massive star formation regions. Symbols in red, green, and blue represent results based on observations via SWAS, and the Odin and Herschel telescopes, respectively. The symbols linked with solid black lines are O_2 detected cases or tentative detection, showing the ranges. Symbols linked by dotted black line represent results of different positions for the same object in the same study. The black arrows suggest the possible lower limit.

The beam-averaged O_2 column density upper limit ($\leqslant 3.3 \times 10^{15} \, cm^{-2}$) we derived in this paper is lower than those values except one (Orion A, $1.9 \times 10^{15} \, cm^{-2}$, Pagani et al. 2003) in massive star formation regions. The abundance upper limit ($\leqslant 6.7 \times 10^{-8}$) we derived is very close to the lowest value (G34.3 +0.2, $\leqslant 5.2 \times 10^{-8}$) based on Odin observations for the 119 GHz O_2 line in Pagani et al. (2003) in a massive star formation region. Compared with our results based on the O_2 487 GHz line, in cold and warm ($\leqslant 50$ K in Pagani et al. 2003) molecular gas, the larger population on the upper level (Goldsmith et al. 2011) and lower frequency of O_2 119 GHz transition will together lead to lower column density and/or abundance upper limit in non-detection cases even when the rms noises are much higher.[22]

The lowest O_2 abundance (upper limit) values (1.3–2.1×10^{-8} and $\leqslant 5.7 \times 10^{-9}$) are based on Herschel observations toward molecular clouds and envelop around NGC 1333 IRAS 4A (a low-mass Class 0 protostar) at 487 GHz, with line width and assumed line widths of 1.3 and $1 \, km \, s^{-1}$ respectively, and the lowest rms noise in all studies of 1.3×10^{-3} K (Yildiz et al. 2013, assuming $T_{kin} = 30$ K).

The O_2 column density upper limits we derived in this paper are lower than upper limit results (see Table E1 in Appendix E) in massive star formation regions the Orion Bar (Melnick et al. 2012) and Rho Oph A (Class 0 protostar IRAS 16293-2422, based on $^{16}O^{18}O$ line, Taquet et al. 2018).

The statistical average O_2 column density and abundance upper limit based on this sample of massive star formation regions under SWAS's beam size can be treated as a kind of average result on the Galactic scale. When converted to the corresponding 1σ value, our O_2 abundance upper limit is lower than those in other extragalactic sources (NGC 6240, Combes et al. 1991; in front of B0218+357, Combes et al. 1997; the center of Mrk 231, Wang et al. 2020.[23])

6. Conclusions

1. We obtained an overall averaged O_2 spectrum for a large sample of Galactic massive star formation regions based on the SWAS survey data. The rms noise per channel of the overall averaged O_2 spectrum is 1.45×10^{-3} K for the overall integration time $t_{total} = 8.67 \times 10^3$ hr. There is no O_2 emission or absorption around the supposed central velocity of the overall averaged O_2 spectrum.

2. At an assumed $T_{kin} = 30$ K, the 3σ average O_2 column density and abundance upper limit for Galactic massive star formation regions based on thermalized O_2 487 GHz line are $3.3 \times 10^{15} \, cm^{-2}$ and 6.7×10^{-8}, respectively. The column density upper limit result we derived in this paper is close to the lowest values in Galactic massive star formation regions in previous studies. The corresponding abundance upper limit is lower than previous results based on SWAS observations and is close to the lowest reported value in massive star formation regions.

3. On a galactic scale, our results confirm that O_2 abundance is very low for Galactic massive star formation regions. The O_2 abundance upper limit we derived in this paper is lower than previous results for extragalactic sources.

Appendix A
C I and O_2 Central Velocity in Galactic O_2 Detection Cases

Observations for C I and O_2 emission toward the same position can be seen in the only two Galactic O_2 detection cases

---

[22] Compared with the rms noise per channel of the overall averaged 487 GHz O_2 spectrum of the sample of the Galactic massive star formation regions in this paper, 1.45×10^{-3} K (based on the observations via SWAS), the rms noises of the 119 GHz O_2 spectra were 5-16 times the former value for the massive star formation sources Orion A, NGC 6334I and G34.3+0.2 observed by Odin in Pagani et al. (2003).

[23] All do not have column density upper limit, see Table E1 in Appendix E.

so far in previous studies, in Rho Oph A and the Orion molecular cloud, which were mentioned in the Introduction. The results do not go against our assumption that C I and O$_2$ lines along the same line of sight have the same central velocity.

In the Rho Oph A O$_2$ detection case, O$_2$'s 119 GHz transition $(1_1–1_0)$ observed by Odin (Larsson et al. 2007), as well as its 487 GHz $(3_3–1_2)$ and 774 GHz $(5_4–3_4)$ transition observed by Herschel (Liseau et al. 2012) all show emission features with central velocities just around 3.5 km s^{-1}. SWAS's C I spectra in the corresponding area ((0, 0) and (0, 1.′6) relative to R. A. = 16:26:23.4, decl. = −24:23:02 (J2000)) show roughly consistent central velocities (3.60 km s^{-1} and 3.44 km s^{-1}, respectively) with the former being O$_2$ observations but with different velocity and spatial resolution (beam size).

A similar situation applies to the O$_2$ detection case in the Orion molecular cloud. In the multi-line O$_2$ observation via Herschel HIFI toward the northwest maximum of H$_2$ rovibrational emission in Orion, the 487 GHz O$_2$ spectrum presents a velocity component whose peak is between 11 and 12 km s^{-1} (10.96 km s^{-1}, FWHM = 3.05 km s^{-1}).[24] This velocity is consistent with those of the transitions between higher energy levels, as 740 GHz (10.96 km s^{-1}, FWHM = 2.91 km s^{-1}) and 1121 GHz (11.87 km s^{-1}, FWHM = 2.87 km s^{-1}) (Goldsmith et al. 2011). In SWAS's beam that covers the same position, the C I 492.161 GHz spectra show a central velocity at 9.69 km s^{-1}. The difference between O$_2$ 487 GHz line and C I 492 GHz line central velocities is acceptable for our assumption.

Appendix B
Calculation of Column Density: Approximations and Assumptions

For a system in thermal equilibrium (TE), the radiative spectrum distribution at temperature T and wavelength ν is (Planck Equation)

$$B_\nu(T) = \frac{2h\nu^3}{c^2} \frac{1}{e^{\frac{h\nu}{kT}} - 1}. \quad (B1)$$

In radio astronomy, in the Rayleigh–Jeans case of $h\nu \ll kT$, the effective source radiation temperature is described by the quasi-Planck function (Kutner & Ulich 1981) as

$$J(\nu, T) = \frac{h\nu}{k} \frac{1}{e^{\frac{h\nu}{kT}} - 1}, \quad (B2)$$

here $J(\nu, T)$ is the radiation temperature of a radio source at (kinetic) temperature T.

For particles in a two-level system with spontaneous emission transition and collisional excitation/deexcitation, the Rayleigh–Jeans approximation can also apply to the line

---

[24] Another velocity component is primarily attributed to the Hot Core.

brightness (temperature) term T_L. For an observed extended source that fills the main beam of the telescope, the main beam brightness temperature $T_{mb} \simeq T_L$.

When the particles are in TE and follow a Boltzmann's distribution, in the optically thin case $\tau \ll 1$, the column density of the upper level is

$$N_u^{\text{quasi-Planck}} = \frac{8\pi\nu^3}{c^3 A_{ul}} \cdot \frac{\frac{1}{e^{\frac{h\nu}{kT_{ex}}} - 1}}{\frac{\frac{h\nu}{k}}{e^{\frac{h\nu}{kT_{kin}}} - 1} - \frac{\frac{h\nu}{k}}{e^{\frac{h\nu}{kT_{bg}}} - 1}} \int T_{mb} dv. \quad (B3)$$

Here T_{ex} is the excitation temperature, $T_{bg} = 2.73$ K is the cosmic background temperature, and A_{ul} is the Einstein A coefficient of the radiative transition from the upper level to the lower level. The total column density is

$$N_{tot}^{\text{quasi-Planck}} = \text{CF} \cdot N_u^{\text{quasi-Planck}}. \quad (B4)$$

CF is the correction factor.

When the upper level is thermalized, $T_{ex} \simeq T_{kin}$. If we replace all T_{ex} terms in Equation (B3) with T_{kin}, that will be the expression adopted for the upper level O$_2$ column density in calculation for O$_2$ total column density in Liseau et al. (2012) when calculating the O$_2$ column density.

In Equation (B3), when $T_{ex} \simeq T_{kin}$, the ratio of the cosmic microwave background radiation temperature term (noted as term A) to the O$_2$ radiation temperature term (notated as term B, B-A is the denominator of the second term on the right-hand side of Equation (B3), and the numerator above them is noted as term C) is

$$R_{bg\text{-to-ex}} = \frac{A}{B} = \frac{\frac{\frac{h\nu}{k}}{e^{\frac{h\nu}{kT_{bg}}} - 1}}{\frac{\frac{h\nu}{k}}{e^{\frac{h\nu}{kT_{ex}}} - 1}} = \frac{e^{\frac{h\nu}{kT_{ex}}} - 1}{e^{\frac{h\nu}{kT_{bg}}} - 1}. \quad (B5)$$

For a given frequency ν, the ratio decreases monotonically as T_{ex} increase. For the O$_2$ 487 GHz line, at an assumed T_{kin} of 30 K ($T_{ex} \simeq T_{kin}$), term A is relatively negligible compared with term B, thus Equation (B3) can be reduced to

$$N_u^{\text{quasi-Planck}-no-bg} = \frac{8\pi\nu^3}{c^3 A_{ul}} \cdot \frac{\frac{1}{e^{\frac{h\nu}{kT_{ex}}} - 1}}{\frac{\frac{h\nu}{k}}{e^{\frac{h\nu}{kT_{ex}}} - 1}} \int T_{mb} dv. \quad (B6)$$

Equation (B6) is analytically equivalent to the expression in common use (Equation (B7)), which actually has term A ignored and the Rayleigh–Jeans approximation adopted for both term B and term C in Equation (B3), when $T_{ex} \simeq T_{kin}$

$$N_u^{\text{quasi-Planck}-no-bg} = N_u^{R-J-no-bg}$$
$$= \frac{8\pi k\nu^2}{hc^3 A_{ul}} \int T_{mb} dv. \quad (B7)$$

The total column density is

$$N_u^{\text{quasi-Planck}-\text{no}-\text{bg}} = \text{CF} \cdot N_u^{R-J-\text{no}-\text{bg}}$$
$$= \text{CF} \cdot \frac{8\pi k\nu^2}{\text{hc}^3 A_{ul}} \int T_{\text{mb}} \text{dv}. \qquad \text{(B8)}$$

Equation (B8) has been adopted in estimations of O_2 column density in earlier studies (Goldsmith et al. 2000, 2002, 2011). When $T_{\text{ex}} \simeq T_{\text{kin}}$, the difference between Equation (B4) (the Quasi-Planck expression) and Equation (B8) (The Rayleigh–Jeans expression) is actually caused by the cosmic microwave background radiation temperature term (term A). Although in our calculation in this paper, $h\nu \ll kT_{\text{kin}}$ does not apply to a frequency as high as 487 GHz for the O_2 (3,3–1,2) transition, considering the derivation above, we adopted Equation (B8) in the total column density calculation for both O_2 and $C^{18}O$.

For total column density calculation, Mangum & Shirley (2015) presented the analysis of the difference caused by the same reason. The results (the lower half of Figure 3 in that paper) show that for frequency of 487 GHz at T_{ex} ($\simeq T_{\text{kin}}$ for thermalized energy level) above 8 K, the difference between the derived total column density in these two cases (Equations (B4) and (B8)) is less than 1%. For $C^{18}O$ $J = 1$–0 at T_{ex} above 30 K, this difference is less than 5% (less than 10% above 20 K).

Appendix C
Corrections and Deviation for Parameters in Calculation for O_2 Column Density and Abundance Upper Limit

C.1. Correction for O_2 rms Noise Per Channel

The baseline noise performance of the overall averaged O_2 spectrum was checked as it was performed in Wang et al. (2024). The "clean" baseline velocity intervals without spikes or ripples in the average O_2 spectra of every observed position were aligned and added up. The rms noise per channel of the overall added up spectrum is 1.13×10^{-3} K, lower than the theoretical value of 1.24×10^{-3} K (calculated according to Goldsmith et al. 2002 and Tolls et al. 2004) by a factor of 1.09.

A similar phenomenon has also been reported in Goldsmith et al. (2000) and Goldsmith et al. (2002). It may be caused by the larger-than-theoretical effective noise bandwidth and has been analyzed in Wang et al. (2024). Thus, we corrected the rms noise per channel of the overall averaged O_2 spectrum from 1.33×10^{-3} K to 1.45×10^{-3} K by multiplying the factor of 1.09.

C.2. Line Width of O_2, $C^{18}O$ and C I

Models for PDF regions suggest that CO and its isotopic variants are generally cospatial and cotemporal with O_2 in star-forming gases (Hollenbach et al. 2009; Draine 2011). The line width of $C^{18}O$ $J = 1$–0 was adopted as that of the supposed O_2 line width to estimate its column density upper limit in a previous study (Pagani et al. 2003). $C^{18}O$ has also been used to estimate O_2 abundance via $X_{C^{18}O}$ (based on $J = 3$–2 or multi-transitions in Pagani et al. 2003; Larsson et al. 2007; Liseau et al. 2012; Yildiz et al. 2013; based on $J = 1$–0 in Goldsmith et al. 2000, 2002; Pagani et al. 2003; Sandqvist et al. 2015 (with $N(\text{H}_2)$ via $C^{18}O$ $J = 1$–0 in Sandqvist et al. 2003)) in previous studies.

In the detected case of O_2 119 GHz emission in Rho Oph A in Larsson et al. (2007), the $C^{18}O$ $J = 3$–2 spectrum shows consistent central velocity and line width with those of the 119 GHz O_2 spectrum despite the very different beam sizes (15″ versus 9′).

The $C^{18}O$ $J = 1$–0 line width can be the proxy of that of the corresponding O_2 spectrum. In this paper, we adopted the line width of the overall averaged C I spectrum as the assumed value for the corresponding $C^{18}O$ $J = 1$–0 and O_2 (3,3–1,2) spectrum.

C I is distributed more extensively than CO isotopic variants through different optical depth (Yamamoto 2017), therefore a larger line width than that of $C^{18}O$ can be expected. In observation cases with different spatial resolutions, the C I spectrum shows larger line width than the $C^{18}O$ low-J transitions.

In SWAS's observations toward Rho Oph A, line width of C I ($^3P_1$–$^3P_0$) is 2.7 km s^{-1} while the $C^{18}O$ (1–0) line toward the same position[25] has a line width of 1.5 km s^{-1} (Goldsmith et al. 2002). Also in this position, the 119 GHz O_2 (1_1–1_0) spectrum[26] has a line width of 1.5 km s^{-1} (Larsson et al. 2007). In the observation toward the molecular cloud core HH24-26 through the James Clerk Maxwell Telescope (JCMT) (Gibb & Little 1998), C I ($^3P_1$–$^3P_0$) spectra have line width larger than that of corresponding $C^{18}O$ (2–1) spectra (with angular resolution 23″ versus 10″) over six different positions within the clump. The line width ratios vary from 1.0 to 2.3. Those observation cases suggest that the C I 492 GHz line is likely to have a larger line width than that of the $C^{18}O$ (1–0) spectrum.

For the seven giant molecular cloud cores in the massive star formation region (see Section 4.2.1) whose parameters were adopted for estimation in this paper, we derived their $C^{18}O$ (1–0) line width from Table 1 in Goldsmith et al. (2000) according to Equation (10) in this paper. The median and average of $C^{18}O$ (1–0) line width are 5.6 and 6.5 ± 4.4 km s^{-1}, respectively. At the same SWAS spatial resolution, the average C I spectra toward individual positions all have larger line width. The median and average line width of C I are 6.2 and 7.8 ± 3.9 km s^{-1}, respectively. The average value of the C I and $C^{18}O$ (1–0) line width ratio for each individual of the seven sources is 1.21 ± 0.25. Based on this average value, we corrected the assumed $C^{18}O$ (1–0) line width from that of the overall averaged C I spectrum (6.3 km s^{-1}) to 5.2 km s^{-1}. We therefore corrected the assumed line width for the overall

---

[25] Obtained through FCRAO and convolved to resolution of 4.′4 FWHM.
[26] At Odin's beamsize of 9′ while covering the whole SWAS beam.

averaged O_2 spectrum to this value as that for $C^{18}O$ (1–0) as well in our estimation for O_2 column density upper limit.

C.3. O_2 Column Density and Abundance Upper Limit at Different T_{kin}

If the O_2 (3,3) level is thermalized, the O_2 column density upper limit is 1.26 times the value at 30 K for $T_{kin} = 15$ K, and 1.0–1.06 times the value at 30 K for $T_{kin} = 20\text{-}40$ K. When the $C^{18}O$ $J = 1$ level is also thermalized, at $T_{kin} = 30$ K, CF(O_2, 3_3)/CF($C^{18}O$,

$J = 1$) = 1.67. For $T_{kin} = 15$ K to 40 K, CF(O_2, 3_3)/CF($C^{18}O$, $J = 1$) = 3.43–1.40. Thus, the O_2 abundance upper limit value can be 0.84–2.05 times the value at 30 K. The O_2 abundance upper limit can be as high as twice the value we derived for $T_{kin} = 30$ K.

Appendix D
Massive Star Formation Regions Analyzed in this Paper

Table D1
Massive Star Formation Regions Analyzed in this Paper

Source	t_{total} (on+off, h)	R.A. Relative to (0,0) (″)	Decl. Relative to (0,0) (″)	R.A. (deg)	Decl. (deg)	l (deg)	b (deg)
CEPHA	88.06	0.00	1.37	344.07	62.03	109.87	2.11
CEPHA	45.75	0.46	192.92	344.07	62.08	109.89	2.16
CEPHA	33.67	−0.15	−192.71	344.07	61.98	109.85	2.07
CEPHA	56.32	192.86	0.56	344.13	62.03	109.89	2.10
CEPHA	48.18	−189.10	−2.21	344.02	62.03	109.85	2.12
CEPHA+15	35.44	−2.47	−3.06	344.07	62.03	109.87	2.11
CEPHA+15-NO	21.64	4.23	−193.87	344.08	61.98	109.85	2.07
CEPHA-30	7.71	1.39	193.08	344.07	62.08	109.89	2.16
CEPHA-30	7.50	0.72	−192.99	344.07	61.98	109.85	2.07
CEPHA-30	6.61	192.55	−1.33	344.13	62.03	109.89	2.10
CEPHA-30	7.68	−190.85	−0.85	344.02	62.03	109.85	2.12
CEPHB	98.18	−0.35	0.34	344.31	62.57	110.20	2.56
CEPHB	89.79	−0.20	384.30	344.31	62.68	110.25	2.65
CEPHB	105.27	195.60	190.65	344.37	62.62	110.25	2.59
CEPHB	93.99	2.68	191.24	344.31	62.63	110.23	2.60
CEPHB	111.88	−194.63	192.82	344.26	62.63	110.20	2.62
CEPHB	91.87	382.49	3.05	344.42	62.57	110.25	2.54
CEPHB	96.21	190.43	3.45	344.36	62.57	110.22	2.55
CEPHB	97.16	−192.26	0.05	344.26	62.57	110.18	2.57
CEPHB	96.32	−2.28	−194.03	344.31	62.52	110.18	2.51
G265.1+1.5	36.02	0.79	1.19	134.85	−43.77	265.15	1.43
G265.1+1.5	19.54	187.82	384.95	134.90	−43.66	265.09	1.53
G265.1+1.5	23.41	2.42	383.31	134.85	−43.66	265.07	1.50
G265.1+1.5	31.03	383.34	193.17	134.95	−43.72	265.16	1.53
G265.1+1.5	31.13	188.78	191.48	134.90	−43.72	265.13	1.50
G265.1+1.5	29.04	−0.79	193.11	134.85	−43.72	265.11	1.47
G265.1+1.5	30.92	−193.97	192.99	134.79	−43.72	265.08	1.44
G265.1+1.5	29.20	383.90	0.37	134.95	−43.77	265.20	1.49
G265.1+1.5	30.28	193.69	−0.99	134.90	−43.77	265.18	1.46
G265.1+1.5	31.24	−192.78	−0.12	134.79	−43.77	265.12	1.40
G265.1+1.5	19.57	385.17	−190.85	134.95	−43.82	265.24	1.46
G265.1+1.5	31.76	192.74	−192.05	134.90	−43.82	265.22	1.43
G265.1+1.5	32.32	1.19	−191.67	134.85	−43.82	265.19	1.40
G265.1+1.5	32.12	−192.11	−193.57	134.79	−43.82	265.16	1.37
G267.9-1.1	65.46	−1.71	2.01	134.80	−47.48	267.93	−1.03
G267.9-1.1	36.13	191.07	191.96	134.85	−47.43	267.92	−0.96
G267.9-1.1	53.92	−1.60	191.77	134.80	−47.43	267.89	−0.99
G267.9-1.1	25.73	−191.22	192.56	134.75	−47.43	267.87	−1.02
G267.9-1.1	37.61	192.26	2.55	134.85	−47.48	267.96	−1.00
G267.9-1.1	20.64	−192.74	1.35	134.75	−47.48	267.91	−1.05
G267.9-1.1	31.46	−383.62	0.32	134.69	−47.48	267.89	−1.08
G267.9-1.1	55.02	190.44	−189.67	134.85	−47.54	268.00	−1.03
G267.9-1.1	17.56	−1.11	−192.66	134.80	−47.54	267.97	−1.06
G267.9-1.1	20.84	−193.89	−193.10	134.75	−47.54	267.95	−1.09

Table D1
(Continued)

Source	t_{total} (on+off, h)	R.A. Relative to (0,0) (″)	Decl. Relative to (0,0) (″)	R.A. (deg)	Decl. (deg)	l (deg)	b (deg)
G267.9-1.1	28.08	−384.92	−193.07	134.69	−47.54	267.93	−1.12
G267.9-1.1	19.18	193.44	−378.92	134.85	−47.59	268.04	−1.07
G267.9-1.1	36.30	2.04	−381.88	134.80	−47.59	268.01	−1.10
G267.9-1.1	35.21	−194.37	−381.83	134.75	−47.59	267.99	−1.12
G291.3-0.7	33.39	381.21	387.34	168.01	−61.22	291.26	−0.62
G291.3-0.7	32.44	193.17	388.59	167.96	−61.22	291.24	−0.63
G291.3-0.7	33.22	575.76	197.89	168.07	−61.28	291.30	−0.66
G291.3-0.7	41.40	383.66	194.76	168.01	−61.28	291.28	−0.67
G291.3-0.7	38.18	192.86	194.82	167.96	−61.28	291.26	−0.68
G291.3-0.7	48.35	−0.13	196.46	167.91	−61.28	291.23	−0.69
G291.3-0.7	55.99	386.48	2.98	168.01	−61.33	291.30	−0.72
G291.3-0.7	20.05	192.83	4.28	167.96	−61.33	291.28	−0.73
G291.3-0.7	30.93	−190.09	3.09	167.85	−61.33	291.23	−0.75
G291.3-0.7	29.25	193.12	−189.23	167.96	−61.38	291.30	−0.78
G291.3-0.7	30.63	1.84	−189.17	167.91	−61.38	291.27	−0.79
G291.3-0.7	68.44	286.86	99.40	167.99	−61.30	291.28	−0.70
G301.1-0.2	67.18	−1.72	2.27	188.86	−63.04	301.12	−0.23
G301.1-0.2	24.19	97.67	3.69	188.89	−63.04	301.13	−0.22
G336.5-1.5	24.47	−3.25	0.54	250.00	−48.86	336.50	−1.47
G336.5-1.5	10.54	189.39	189.53	250.05	−48.80	336.56	−1.46
G336.5-1.5	11.48	−3.54	192.22	250.00	−48.80	336.54	−1.43
G336.5-1.5	10.23	−192.93	189.58	249.95	−48.80	336.51	−1.41
G336.5-1.5	10.25	192.17	−2.02	250.05	−48.86	336.52	−1.50
G336.5-1.5	10.47	−194.77	−2.01	249.95	−48.86	336.47	−1.44
G336.5-1.5	14.17	−384.85	0.48	249.89	−48.86	336.45	−1.42
G336.5-1.5	10.44	190.62	−193.72	250.05	−48.91	336.48	−1.53
G336.5-1.5	17.26	−0.14	−188.44	250.00	−48.91	336.46	−1.51
G336.5-1.5	10.25	−195.10	−193.51	249.95	−48.91	336.43	−1.48
G336.5-1.5	14.96	1.70	−381.99	250.00	−48.96	336.42	−1.54
MONR2	37.55	−4.53	4.51	91.92	−6.39	213.70	−12.63
MONR2	18.32	194.59	189.35	91.97	−6.34	213.67	−12.56
MONR2	18.42	−0.11	190.57	91.92	−6.34	213.65	−12.61
MONR2	13.55	384.37	−1.18	92.02	−6.39	213.75	−12.53
MONR2	13.88	192.27	−0.01	91.97	−6.39	213.72	−12.58
MONR2	15.66	−191.75	−2.12	91.86	−6.39	213.67	−12.68
MONR2	18.19	191.42	−193.48	91.97	−6.44	213.77	−12.61
MONR2	13.86	1.34	−189.71	91.92	−6.44	213.75	−12.65
MONR2	11.74	−193.44	−194.49	91.86	−6.45	213.72	−12.70
MONR2	35.10	97.47	45.63	91.94	−6.38	213.70	−12.60
N2264SC-S	22.72	−0.05	−1.76	100.29	9.48	203.32	2.05
N2264SC-S	19.55	386.71	2.83	100.40	9.49	203.37	2.15
N2264SC-S	44.68	192.45	2.40	100.35	9.49	203.35	2.10
N2264SC-S	27.92	−189.17	−0.50	100.24	9.49	203.30	2.01
N2264SC-S	17.46	191.83	−193.03	100.35	9.43	203.40	2.08
N2264SC-S	29.04	−4.39	−193.74	100.29	9.43	203.37	2.03
N2264SC-S	17.97	−192.31	−193.58	100.24	9.43	203.35	1.98
NGC 3576	39.58	2.77	6.39	167.98	−61.31	291.28	−0.71
NGC 3576	29.46	2.03	195.14	167.98	−61.25	291.26	−0.66
NGC 3576	22.32	387.40	1.47	168.08	−61.31	291.32	−0.69
NGC 3576	29.32	194.14	3.60	168.03	−61.31	291.30	−0.70
NGC 3576	32.69	−188.81	4.94	167.92	−61.31	291.25	−0.72
NGC 3576	23.93	195.27	−186.40	168.03	−61.36	291.32	−0.75
NGC 3576	29.67	0.32	−187.52	167.98	−61.36	291.29	−0.76
NGC 3576	18.14	−192.63	−187.87	167.92	−61.36	291.27	−0.77
NGC 6334A	26.57	0.44	−0.65	260.08	−35.91	351.25	0.66
NGC 6334A	10.61	188.46	−0.33	260.14	−35.91	351.27	0.63
NGC 6334A	14.13	−191.75	0.49	260.03	−35.91	351.22	0.70
NGC 6334A	12.26	−385.37	2.66	259.98	−35.91	351.20	0.73

Table D1
(Continued)

Source	t_{total} (on+off, h)	R.A. Relative to (0,0) (″)	Decl. Relative to (0,0) (″)	R.A. (deg)	Decl. (deg)	l (deg)	b (deg)
NGC 6334C	29.29	−0.18	−3.57	260.12	−35.87	351.30	0.67
NGC 6334C	10.76	−1.07	191.79	260.12	−35.82	351.34	0.70
NGC 6334C	13.07	−194.35	192.15	260.06	−35.82	351.32	0.73
NGC 6334C	11.99	382.82	0.96	260.22	−35.87	351.35	0.60
NGC 6334C	9.96	189.72	−0.91	260.17	−35.87	351.32	0.63
NGC 6334C	10.45	−197.02	−0.99	260.06	−35.87	351.27	0.70
NGC 6334C	48.62	−126.33	−165.74	260.08	−35.92	351.24	0.66
NGC 6334D	27.30	2.58	−0.87	260.18	−35.79	351.39	0.67
NGC 6334D	12.70	384.45	1.25	260.28	−35.79	351.44	0.60
NGC 6334D	10.32	190.89	1.62	260.23	−35.79	351.41	0.64
NGC 6334D	10.65	−191.96	0.60	260.12	−35.79	351.36	0.71
NGC 6334D	11.36	383.20	−190.09	260.28	−35.84	351.39	0.57
NGC 6334D	13.59	190.53	−190.21	260.23	−35.84	351.37	0.61
NGC 6334D	11.17	−2.05	−190.42	260.18	−35.84	351.35	0.64
NGC 6334I	238.71	−2.41	−3.34	260.22	−35.75	351.44	0.67
NGC 6334I	12.63	191.43	192.44	260.27	−35.70	351.51	0.66
NGC 6334I	10.48	−1.52	191.94	260.22	−35.70	351.49	0.70
NGC 6334I	13.44	191.43	0.80	260.27	−35.75	351.47	0.63
NGC 6334I	12.29	−194.02	0.81	260.17	−35.75	351.42	0.70
NGC 6334V	14.95	0.18	−1.35	259.99	−35.97	351.16	0.69
NGC 6334V	13.17	580.28	6.32	260.15	−35.97	351.24	0.59
NGC 6334V	12.45	384.22	1.68	260.10	−35.97	351.21	0.62
NGC 6334V	10.54	190.02	−1.26	260.05	−35.97	351.18	0.66
NGC 6334V	10.50	−192.60	1.88	259.94	−35.97	351.14	0.73
NGC 6334V	12.32	192.60	−188.39	260.05	−36.02	351.14	0.63
NGC 6334V	12.50	−2.58	−190.08	259.99	−36.02	351.12	0.66
S106	16.02	−1.31	1.10	306.89	37.38	76.39	−0.64
S106	33.80	−0.35	192.60	306.89	37.43	76.44	−0.61
S106	31.02	191.98	3.68	306.94	37.38	76.42	−0.67
S106	15.93	−95.33	1.48	306.86	37.38	76.38	−0.62
S106	15.38	−197.04	2.54	306.83	37.38	76.37	−0.60
S106	27.38	−384.39	3.68	306.78	37.38	76.35	−0.57
S106	35.32	0.44	−187.83	306.89	37.33	76.35	−0.67
S140	274.69	−0.25	−0.47	334.82	63.31	106.79	5.31
S140	21.36	193.27	191.56	334.87	63.37	106.84	5.34
S140	36.96	1.43	192.54	334.82	63.37	106.82	5.36
S140	25.88	−189.77	190.72	334.77	63.37	106.80	5.37
S140	20.89	194.55	−1.46	334.88	63.31	106.82	5.30
S140	56.25	−192.04	−0.84	334.77	63.31	106.77	5.33
S140	18.31	194.51	−192.84	334.88	63.26	106.79	5.25
S140	54.83	1.43	−194.31	334.82	63.26	106.77	5.27
S140	67.40	−189.28	−193.36	334.77	63.26	106.75	5.28
W3	34.87	−3.18	3.85	36.37	62.10	133.69	1.21
W3	22.49	189.82	193.99	36.43	62.15	133.70	1.27
W3	21.27	−3.75	193.83	36.37	62.15	133.68	1.26
W3	19.48	381.79	0.71	36.48	62.10	133.74	1.23
W3	27.87	−190.96	3.12	36.32	62.10	133.67	1.20
W3	9.39	187.52	−187.93	36.43	62.05	133.74	1.17
W3	27.69	0.75	−188.85	36.37	62.05	133.71	1.16
G10.47+0.03	17.04	−1.76	0.90	272.15	−19.87	10.47	0.03
G10.47+45	30.27	3.10	−0.69	272.15	−19.87	10.47	0.03
G10.6-0.4	61.48	−3.72	1.29	272.62	−19.93	10.62	−0.38
G10.6-0.4-NO1	12.76	0.41	4.24	272.62	−19.93	10.62	−0.38
G12.21-0.01	22.14	0.73	0.04	273.17	−18.41	12.21	−0.10
G23.95+0.15	38.64	−0.44	1.11	278.61	−7.91	23.96	0.14
G268.4-0.9	132.84	0.59	1.84	135.48	−47.73	268.42	−0.85
G269.2-1.1	24.60	−0.25	4.66	135.89	−48.47	269.15	−1.12
G269.2-1.1+30	139.94	0.87	−0.54	135.89	−48.47	269.15	−1.13

Table D1
(Continued)

Source	t_{total} (on+off, h)	R.A. Relative to (0,0) ($''$)	Decl. Relative to (0,0) ($''$)	R.A. (deg)	Decl. (deg)	l (deg)	b (deg)
G31.41+0.31	27.62	1.10	3.57	281.89	−1.21	31.41	0.31
G327.3-0.5	22.35	0.48	5.71	238.29	−54.62	327.30	−0.58
G333.1-0.4	77.00	3.56	−0.05	245.26	−50.59	333.13	−0.43
G34.3+0.1	86.64	0.66	−1.06	283.33	1.25	34.26	0.15
G34.3+0.1+15	41.01	−0.66	1.80	283.33	1.25	34.26	0.15
G48.61+0.02	8.66	1.71	2.27	290.13	13.92	48.61	0.02
G59.78+0.06	12.96	−0.60	5.45	295.80	23.73	59.78	0.06
G60.89-0.13	3.48	−2.10	1.15	296.58	24.59	60.88	−0.13
14498-5856-60	62.56	−3.69	2.43	223.42	−59.15	318.05	0.09
14498-5856	36.90	−2.14	1.65	223.42	−59.15	318.05	0.09
AFGL961	2.90	−4.79	−4.20	98.66	4.19	207.28	−1.82
CEPHEUS-E	63.63	−0.83	0.78	345.80	61.71	110.48	1.48
CEPHEUS-E-30	39.21	−2.60	0.25	345.80	61.71	110.48	1.48
GL490	135.17	0.36	−2.29	51.91	58.78	142.00	1.82
GL490-60	43.82	0.39	3.60	51.91	58.78	142.00	1.82
IR20126-30	33.50	1.74	−2.95	303.61	41.22	78.12	3.63
IRAS08576-43	45.18	0.67	0.60	134.86	−43.76	265.15	1.44
IRAS20126	78.91	1.40	0.48	303.61	41.23	78.12	3.63
IRAS22566	40.76	−1.65	2.51	344.70	58.76	108.76	−0.98
IRAS22566-30	42.61	−0.80	0.77	344.70	58.75	108.76	−0.98
K3-50	49.48	1.56	3.19	300.44	33.55	70.29	1.60
M8E	35.17	3.30	0.05	271.23	−24.44	6.05	−1.45
NGC 7538IRS1	37.62	1.21	−4.27	348.44	61.47	111.54	0.78
NGC 7538IRS9	101.03	6.40	1.80	348.51	61.46	111.57	0.75
ON2S	81.15	−2.18	3.41	305.42	37.41	75.75	0.34
RAFGL7009S	72.68	3.39	0.46	278.59	−5.99	25.65	1.05
RCW34	88.53	2.21	3.67	134.13	−43.08	264.29	1.49
RCW34-NO1	97.75	0.32	−0.04	134.13	−43.08	264.29	1.48
RCW34-NO1-30	38.77	−1.81	1.88	134.13	−43.08	264.29	1.48
S152	29.20	−1.48	3.38	344.68	58.76	108.76	−0.97
S252A	19.72	−4.24	−2.53	92.15	20.65	189.78	0.35
S255	31.47	−1.57	−0.75	93.22	17.99	192.60	−0.05
S87	52.31	1.60	−0.11	296.59	24.60	60.90	−0.13
W3IRS5	21.46	1.36	−1.85	36.42	62.10	133.72	1.21
W3-OH	50.18	−2.56	1.92	36.76	61.87	133.95	1.06
W51+30	5.85	0.00	1.74	290.93	14.51	49.49	−0.38
W51	238.03	1.81	−3.66	290.93	14.51	49.49	−0.38
G291.3-0.7	123.58	−0.45	0.37	167.91	−61.33	291.25	−0.74
NGC 7538	87.07	1.42	−1.83	348.45	61.45	111.54	0.75
W49	740.84	−1.19	3.39	287.56	9.11	43.17	0.01
W49-NO1	34.91	−0.22	−0.82	287.56	9.11	43.17	0.01
G274.1-1.14	6.74	−2.37	−1.10	141.11	−51.99	274.00	−1.14
M17SW	217.88	−0.42	2.47	275.09	−16.21	15.01	−0.68

Appendix E
Molecular Oxygen Column and Abundance Upper Limit in Literature

Table E1
O_2 Column and Abundance Upper Limit In Literature

Source	N_{O_2} Upper Limit	X_{O_2} Upper Limit	Temperature	Note	Telescope	References
In Galaxy						
NGC 2024	⋯	$<6.1 \times 10^{-7}$	35 K	3σ	SWAS	derived from Goldsmith et al. (2000)
NGC 2071	⋯	$<1.5 \times 10^{-6}$	20 K	3σ	SWAS	derived from Goldsmith et al. (2000)
NGC 2071	$<2.6 \times 10^{15}$	$<1.5 \times 10^{-7}$	20 K	3σ	Odin	Pagani et al. (2003)
Mon R2	⋯	$<1.3 \times 10^{-6}$	40 K	3σ	SWAS	derived from Goldsmith et al. (2000)
NGC 2264	⋯	$<5.6 \times 10^{-7}$	30 K	3σ	SWAS	derived from Goldsmith et al. (2000)
Sgr B2	⋯	$<4.6 \times 10^{-7}$	30 K	3σ	SWAS	derived from Goldsmith et al. (2000)
W33	⋯	$<5.4 \times 10^{-7}$	23 K	3σ	SWAS	derived from Goldsmith et al. (2000)
W49	⋯	$<1.9 \times 10^{-6}$	25 K	3σ	SWAS	derived from Goldsmith et al. (2000)
W51	⋯	$<3.6 \times 10^{-7}$	30 K	3σ	SWAS	derived from Goldsmith et al. (2000)
S140	⋯	$<1.0 \times 10^{-6}$	30 K	3σ	SWAS	derived from Goldsmith et al. (2000)
DR 21	⋯	$<1.5 \times 10^{-6}$	30 K	3σ	SWAS	derived from Goldsmith et al. (2000)
DR 21(OH)	⋯	$<1.4 \times 10^{-6}$	30 K	3σ	SWAS	derived from Goldsmith et al. (2000)
Cep A	⋯	$<9.4 \times 10^{-7}$	30 K	3σ	SWAS	derived from Goldsmith et al. (2000)
NGC 7538	⋯	$<9.7 \times 10^{-7}$	25 K	3σ	SWAS	derived from Goldsmith et al. (2000)
M17SW	⋯	$<3.7 \times 10^{-7}$	40 K	3σ	SWAS	derived from Goldsmith et al. (2000)
M17SW	$<7.3 \times 10^{15}$	$<5.7 \times 10^{-7}$	50 K	3σ	Odin	Pagani et al. (2003)
TMC-1	⋯	$<2.7 \times 10^{-6}$	10 K	3σ	SWAS	derived from Goldsmith et al. (2000)
TMC1-NH3	$<6.8 \times 10^{14}$	$<7.7 \times 10^{-8}$	10 K	3σ	Odin	Pagani et al. (2003)
L134N	⋯	$<2.9 \times 10^{-6}$	10 K	3σ	SWAS	derived from Goldsmith et al. (2000)
L134N-NH3	$<1.1 \times 10^{15}$	$<1.7 \times 10^{-7}$	10 K	3σ	Odin	Pagani et al. (2003)
NGC 6334I	$<5.0 \times 10^{15}$	$<7.1 \times 10^{-8}$	50 K	3σ	Odin	Pagani et al. (2003)
G0.26-0.01	$<5.6 \times 10^{16}$	$<7.6 \times 10^{-7}$	20? K	3σ	Odin	Pagani et al. (2003)
S68FIRS1	$<1.6 \times 10^{15}$	$<9.7 \times 10^{-8}$	25 K	3σ	Odin	Pagani et al. (2003)
G34.3+0.2	$<5.2 \times 10^{15}$	$<5.2 \times 10^{-8}$	30 K	3σ	Odin	Pagani et al. (2003)
NGC 1333	⋯	$<1.0 \times 10^{-6}$	25 K	3σ	SWAS	derived from Goldsmith et al. (2000)
NGC 1333 IRAS 4 Protostar	$<1.2 \times 10^{15}$	$<5.7 \times 10^{-9}$	30 K	3σ	Herschel	Yildiz et al. (2013)
NGC 1333 IRAS 4 cloud	$(2.8–4.3) \times 10^{15}$	$(1.3–2.1) \times 10^{-8}$	30 K	tentative detection, 4.5σ	Herschel	Yildiz et al. (2013)
IRAS16293-2422	$<1.7 \times 10^{15}$	$<1.2 \times 10^{-7}$	30 K	3σ	Odin	Pagani et al. (2003)
IRAS16293-2422	$<9 \times 10^{19}$	⋯	$T_{ex} = 125–200$ K	3σ	ALMA	Taquet et al. (2018)
Rho Oph A	⋯	$<2.6 \times 10^{-7}$	30 K	3σ	SWAS	derived from Goldsmith et al. (2000)
Rho Oph A	2.3×10^{16}	$<1.0–1.5 \times 10^{-5}$	40 K	tentative detection	SWAS	Goldsmith et al. (2002)
Rho Oph A	$<3.4 \times 10^{15}$	$<9.3 \times 10^{-8}$	30 K	3σ	Odin	Pagani et al. (2003)

Table E1
(Continued)

Source	N_{O_2} Upper Limit	X_{O_2} Upper Limit	Temperature	Note	Telescope	References
Rho Oph A	1×10^{15}	5×10^{-8}	30 K	5.6σ, detection	Odin	Larsson et al. (2007)
Rho Oph A	$(3–6) \times 10^{15}$	$\sim 5 \times 10^{-8}$, (or more higher in colder region)	>50 K (or <30 K)	3σ	Herschel	Liseau et al. (2012)
Orion H$_2$ Peak 1 (Orion NH$_3$ Peak A)	6.5×10^{16} (4.6×10^{18})	$(0.3–7.3) \times 10^{-6}$ (1.3×10^{-6})	65-120 K $(\geqslant 180$ K)	detection	Herschel	Goldsmith et al. (2011)
Orion bar	$<1 \times 10^{16}$ $(\leqslant 4 \times 10^{15})$	... ...	$\leqslant 100$ K $\leqslant 100$ K	3σ 3σ	Herschel	Melnick et al. (2012)
Orion H$_2$ Peak 1 (Hot Core)	1.1×10^{18} $(1.2–1.9) \times 10^{17}$	$(0.9–1.5) \times 10^{-7}$	$(\sim 30$ K) $(150–300$ K)	detection $(1\sigma$ abundance)	Herschel	Chen et al. (2014)
L429	$<1.1 \times 10^{16}$	$<9.2 \times 10^{-8}$ $(<1.2 \times 10^{-6})$	7 K	3σ (assuming beam dilution factor)	Herschel	Wirström et al. (2016)
Oph D	$<1.2 \times 10^{16}$	$<1.1 \times 10^{-7}$ $(<1.3 \times 10^{-6})$	7 K	3σ (assuming beam dilution factor)	Herschel	Wirström et al. (2016)
L1544	$<8.2 \times 10^{15}$	$<6.3 \times 10^{-8}$ $(<1.6 \times 10^{-6})$	7 K	3σ (assuming beam dilution factor)	Herschel	Wirström et al. (2016)
L694-2	$<1.8 \times 10^{16}$	$<1.6 \times 10^{-7}$ $(<1.3 \times 10^{-6})$	7 K	3σ (assuming beam dilution factor)	Herschel	Wirström et al. (2016)
Sgr A +20–50 km s^{-1}	$\leqslant 6 \times 10^{16}$	$\leqslant 1.2 \times 10^{-7}$		3σ	Herschel	Sandqvist et al. (2008)
Sgr A (Scutum Arm) (−30 km s^{-1} Arm)	$<1.4 \times 10^{16}$	$<5 \times 10^{-8}$ $<(10^{-6}–10^{-4})$ $(<10^{-5}–10^{-4})$	80 K (30 K) (30 K)	3σ 3σ 3σ	Herschel	Sandqvist et al. (2015)
			Extragalactic			
SMC	$<2 \times 10^{15}$	$<1.3 \times 10^{-6}$		3σ	Odin	Wilson et al. (2005)
NGC 6240	$<1.5 \times 10^{16}$	$<1 \times 10^{-6}$	15 K	1σ	IRAM 30 m	Combes et al. (1991)
B0218+357 (in front of)	$<8.9 \times 10^{16}$	$<2 \times 10^{-3}$		1σ (O$_2$/CO)	Nobeyama	Combes et al. (1997)
Mrk 231 (2 kpc in center)		$<8 \times 10^{-8}$		1σ	IRAM 30 m	Wang et al. (2020)
Mrk 231 (outflow)		$>1 \times 10^{-4}$	$T_{ex} =$ 15 K or higher	detection		

ORCID iDs

Bing-Ru Wang ⓘ https://orcid.org/0009-0001-8411-5096
Di Li ⓘ https://orcid.org/0000-0003-3010-7661
Paul F. Goldsmith ⓘ https://orcid.org/0000-0002-6622-8396
Jingwen Wu ⓘ https://orcid.org/0000-0001-7808-3756
Chao-Wei Tsai ⓘ https://orcid.org/0000-0002-9390-9672
Donghui Quan ⓘ https://orcid.org/0000-0003-4811-2581
Xia Zhang ⓘ https://orcid.org/0000-0003-4843-8944
Junzhi Wang ⓘ https://orcid.org/0000-0001-6106-1171
Gary J. Melnick ⓘ https://orcid.org/0000-0002-6025-0680
Jin-Zeng Li ⓘ https://orcid.org/0000-0002-9331-8194
Gary A. Fuller ⓘ https://orcid.org/0000-0001-8509-1818
Jinjin Xie ⓘ https://orcid.org/0000-0002-2738-146X

References

Bergin, E. A., & Melnick, G. J. 2005, in Astrochemistry: Recent Successes and Current Challenges, Proc. of the 231st Symp. of the Int. Astronomical Union, ed. D. C. Lis, G. A. Blake, & E. Herbst (Cambridge: Cambridge Univ. Press), 309

Brown, J., & Carrington, A. 2003, Rotational Spectroscopy of Diatomic Molecules (Cambridge: Cambridge Univ. Press)
Chen, J.-H., Goldsmith, P. F., Serena, V., et al. 2014, ApJ, 793, 111
Combes, F., Casoli, F., Encrenaz, P., et al. 1991, A&A, 248, 607
Combes, F., Wiklind, T., & Nakai, N. 1997, A&A, 327, L17
Dalgarno, A., & McCray, R. A. 1972, ARA&A, 10, 375
Draine, B. T. 2011, Physics of the Interstellar and Intergalactic Medium (Princeton: Princeton Univ. Press)
Drouin, B. J., Yu, S., Miller, C. E., et al. 2010, JQSRT, 111, 1167
Frerking, M. A., Langer, W. D., & Wilson, R. W. 1982, ApJ, 262, 590
Frisk, U., Hagström, M., Ala-Laurinaho, J., et al. 2003, A&A, 402, L27
Gibb, A. G., & Little, L. T. 1998, MNRAS, 295, 299
Goldsmith, P. F., & Langer, W. D. 1978, ApJ, 222, 881
Goldsmith, P. F., Li, D., Bergin, E. A., et al. 2002, ApJ, 576, 814
Goldsmith, P. F., Liseau, R., Bell, T. A., et al. 2011, ApJ, 737, 96
Goldsmith, P. F., Melnick, G. J., Bergin, E. A., et al. 2000, ApJL, 539, L123
Goldsmith, P. F., Snell, R. L., Erickson, N. R., et al. 1985, ApJ, 289, 613
Goldsmith, P. F., & Young, J. S. 1989, ApJ, 341, 718
Gordy, W., & Cook, R. L. 1984, Microwave Molecular Spectra (Techniques of Chemistry) XVIII(3rd; New York: Wiley)
Heiles, C. 1971, ARA&A, 9, 293
Herbst, E., & Klemperer, W. 1973, ApJ, 185, 505
Hollenbach, D., Kaufman, M. D., Bergin, E. A., et al. 2009, ApJ, 690, 1497
Kaiser, R. I., Eich, G., Gabrysch, A., et al. 1999, A&A, 346, 340
Kutner, M. L., & Ulich, B. L. 1981, ApJ, 250, 341

Langer, W. 1976, ApJ, 206, 699

Larsson, B., Liseau, R., Pagani, L., et al. 2007, A&A, 466, 999

Liseau, R., Goldsmith, P. F., Larsson, B., et al. 2012, A&A, 541, A73

Listz, H. S., & Vanden Bout, P. A. 1985, ApJ, 291, 178

Mangum, J. G., & Shirley, Y. L. 2015, PASP, 127, 266

Maréchal, P., Viala, Y. P., & Benayoun, J. J. 1997, A&A, 324, 221

Melnick, G. J. 1995, in Airborne Astronomy Symp. on the Galactic Ecosystem: From Gas to Stars to Dust, Astronomical Society of the Pacific Conf. Series, ed. M. R. Haas, J. A. Davidson, & E. F. Erickson (San Francisco: ASP), 673

Melnick, G. J., & Kaufman, M. J. 2015, ApJ, 806, 227

Melnick, G. J., Stauffer, J. R., Ashby, M. L. N., et al. 2000, ApJL, 539, L77

Melnick, G. J., Tolls, V., Goldsmith, P. F., et al. 2012, ApJ, 752, 26

Neufeld, D. A., Lepp, S., & Melnick, G. J. 1995, ApJS, 100, 132

Nordh, H. L., von Schéele, F., Frisk, U., et al. 2003, A&A, 402, L21

Pagani, L., Olofsson, A. O. H., Bergman, P., et al. 2003, A&A, 402, L77

Pilbratt, G. L., Riedinger, J. R., Passvogel, T., et al. 2010, A&A, 518, L1

Sandqvist, A., Bergman, P., Black, J. H., et al. 2003, A&A, 402, L63

Sandqvist, A., Larsson, B., Hjalmarson, Å., et al. 2008, A&A, 482, 849

Sandqvist, A., Larsson, B., Hjalmarson, Å., et al. 2015, A&A, 584, A118

Taquet, V., Van Dishoeck, E. F., Swayne, M., et al. 2018, A&A, 618, A11

Tielens, A. G. G. M. 2013, RvMP, 85, 1021

Tolls, V., Melnick, G. J., Ashby, M. L. N., et al. 2004, ApJS, 152, 137

Van der Tak, F. F. S., Black, J. H., Schöier, F. L., Jansen, D. J., & van Dishoeck, E. F. 2007, A&A, 468, 627

van Dishoeck, E. F., Herbst, E., & Neufeld, D. A. 2013, ChRv, 113, 9043

Vastel, C., Polehampton, E. T., Baluteau, J.-P., et al. 2002, ApJ, 581, 315

Wang, B.-R., Li, D., Goldsmith, P. F., et al. 2024, RAA, 24, 065026, #

Wang, J., Li, D., Goldsmith, P. F., et al. 2020, ApJ, 889, 129

Wang, S., Li, A., & Jiang, B. W. 2015, MNRAS, 454, 569

Whittet, D. C. B. 2010a, LPICo, 1538, 5194

Whittet, D. C. B. 2010b, ApJ, 710, 1009

Whittet, D. C. B., Goldsmtih, P. F., & Pineda, J. L. 2010, ApJ, 720, 259

Wilson, C. D., Olofsson, A. O. H., Pagani, L., et al. 2005, A&A, 433, L5

Wirström, E. S., Charnley, S. B., Cordiner, M. A., et al. 2016, ApJ, 830, 102

Yamamoto, S. 2017, Introduction to Astrochemistry: Chemical Evolution from Interstellar Clouds to Star and Planet Formation (Tokyo: Springer)

Yildiz, U. A., Acharyya, K., Goldsmith, P. F., et al. 2013, A&A, 558, A58

Zhang, X., Quan, D., & Esimbek, J. 2020, ChJCP, 33, 107